



SORAS (Stratospheric Ozone Radiometer in Seoul), a ground-based 110 GHz microwave radiometer for measuring the stratospheric ozone vertical profile

Soohyun Ka¹ and Jung Jin Oh^{1,2}

¹Research Institute of Global Environment, Sookmyung Women's University, Seoul, 04310, South Korea

²Department of Chemistry, Sookmyung Women's University, Seoul, 04310, South Korea

Correspondence: Jung Jin Oh (jjinoh@sookmyung.ac.kr)

Received: 17 June 2024 – Discussion started: 3 September 2024

Revised: 29 December 2024 – Accepted: 21 January 2025 – Published: 13 March 2025

Abstract. A ground-based 110 GHz radiometer was designed to measure the stratospheric ozone vertical profile by observing the 110.836 GHz ozone emission spectrum, and the instrument is operational at Sookmyung Women's University (37.54° N, 126.97° E) in Seoul, South Korea. In this paper, we detail the instrumental design, calibration procedures, correction methods, and the retrieved ozone vertical profile. The instrument is a heterodyne total power radiometer. It down-converts the observed 110.836 GHz ozone frequency to 0.609 GHz, with a frequency resolution of 61 kHz and a bandwidth of 830 MHz. The spectral intensity is digitized using a fast-Fourier-transform spectrometer. For hot-cold calibration, we use microwave absorbers at room temperature and liquid nitrogen as calibration targets. Tropospheric opacity is corrected using the continuous tipping curve calibration. The measured opacities were compared with simulated values from the Korea Local Analysis and Prediction System (KLAPS) data. Additionally, since 2016, the stratospheric ozone profiles over Seoul have been demonstrated for the vertical range of 100–0.3 hPa (16–70 km), with validation performed by comparing them to the ozone profiles from the Microwave Limb Sounder (MLS) on the AURA satellite.

1 Introduction

Ozone is a trace gas in the atmosphere, with the highest concentrations found in the lower to middle stratosphere. Commonly referred to as the ozone layer, it is a key fac-

tor in global warming and is crucial for absorbing significant amounts of solar UV-B radiation. Ozone is mainly formed by photochemistry in the upper stratosphere (Prather, 1981) and is transported to the rest of the atmosphere. As the ozone in the lower and middle stratosphere has a relatively long lifetime, its distribution is primarily influenced by atmospheric dynamics. The discovery of the ozone hole over the South Pole (Farman et al., 1985) was a major global issue, prompting the 1987 Montreal Protocol to limit halogen gas emissions. Consequently, the overall abundance of ozone-depleting substances (ODSs) in the atmosphere has decreased since the late 1990s, and total ozone in the Antarctic is showing signs of recovery (World Meteorological Organization (WMO), 2022). Likewise, recovery of ozone in the upper stratosphere outside of polar regions has been noted, but trends in the lower and middle stratosphere remain unclear. However, some studies suggest continued ozone depletion in the lower and middle stratosphere over the northern midlatitudes. (Steinbrecht et al., 2017; Ball et al., 2018; Bernet et al., 2019; Szeląg et al., 2020). Since the trends in ozone vertical distribution above specific latitude regions have differed from those of the total ozone column, it is essential to monitor the vertical ozone profile up to the upper stratosphere and even the mesosphere. This monitoring is crucial for understanding stratospheric dynamics and enhancing future climate change predictions.

The ground-based microwave radiometer in this study is a completely passive instrument that measures the vertical profile in the stratosphere, even up to the lower mesosphere, by detecting rotational emissions from trace gases (Parrish et

al., 1988), with permanent electric or magnetic dipole moments such as ozone (Hocke et al., 2007; Fernandez et al., 2015b), water vapor (H_2O) (Deuber et al., 2004; Straub et al., 2010; De Wachter et al., 2011; Gomez et al., 2012), chlorine monoxide (ClO) (Solomon et al., 2000; Connor et al., 2013; Nedoluha et al., 2020), nitric oxide (NO) (Newnham et al., 2011), carbon monoxide (CO) (Straub et al., 2013), and so on. The zonal wind profile in the middle atmosphere (Rüfenacht et al., 2012) and the tropospheric temperature and humidity profiles (Massaro et al., 2015) are observed by the ground-based microwave radiometer.

The stratospheric ozone profiles measured by the ground-based microwave radiometer have a high temporal resolution from continuous monitoring. It enables studies on the transport or dynamics of the middle atmosphere by tracking ozone distribution. The diurnal cycles of stratospheric ozone relative to local solar time have been studied with an hourly resolution (Parrish et al., 2014; Studer et al., 2014; Maillard Barras et al., 2020). The polar vortex displacement towards the midlatitudes was studied through short-term fluctuations in ozone measurements taken at 30 min intervals (Moreira et al., 2018). Moreover, there are studies of a long-term natural variability in the stratospheric ozone caused by the annual and semiannual oscillations (AO and SAO), the quasi-biennial oscillation (QBO), El Niño–Southern Oscillation (ENSO), and the solar activity cycle (Moreira et al., 2016).

In this paper, we introduce the ground-based 110.836 GHz microwave radiometer named SORAS (Stratospheric Ozone Radiometer in Seoul), designed to measure the vertical distribution of stratospheric ozone. This instrument detects the spontaneous radiation emitted during the 6_{15} – 6_{06} rotational transition. It has been developed and is operated at the Research Institute of Global Environment (RIGE) of Sookmyung Women's University (SMWU; 37.54° N, 126.97° E) in Seoul, South Korea. Notably, since 2015, RIGE at SMWU has been designated as a commissioned observatory for climate change by the Korea Meteorological Administration (KMA). This designation underscores the critical role of SORAS in monitoring the stratosphere, contributing to national climate change observation.

With the first microwave radiometer developed in South Korea for stratospheric monitoring, we have implemented multiple hardware modifications and conducted numerous tests to determine the most effective calibration and data correction methods. When SORAS was first developed in 2008, it was configured as a double-sideband system, which differs from its current configuration. Issues with spectral artifacts and suboptimal data correction existed. However, improvements have been made, and observations as stable as the current data have been consistently achieved since 2016.

In the following sections, we describe the stable version of the radiometer post-2016. Section 2 provides instrumental descriptions. Section 3 presents the spectroscopy, calibration, and corrections for SORAS measurements. Section 4 shows

the retrieved ozone profile from SORAS measurements and the validation with AURA Microwave Limb Sounder (MLS) ozone data. Section 5 summarizes the conclusions of this study.

2 Instrumentation

SORAS is a 110 GHz single-sideband heterodyne receiver. It operates at room temperature in an indoor laboratory (Fig. 1). The indoor environment enables the instrument to operate continuously, regardless of weather conditions. The radiometer consists of a quasi-optical part with mirrors and an antenna, a front end with microwave components, and a back end with a spectrometer.

The details of SORAS are described in Fig. 2. The quasi-optical system comprises a rotating plane mirror of an oval shape, an ellipsoidal mirror, and a corrugated horn antenna. The rotating plane mirror controls the selection of the measurement target, with a step angle set to 0.18°. This mirror wobbles continuously back and forth during measurements to suppress standing waves between optical components, which are generated by the phase overlap of propagating forward and backward waves. The ellipsoidal mirror, positioned at 45° off axis, is designed to focus the incident radiation on the corrugated horn antenna, which has a beam waist of 7 mm at 110 GHz. The corrugated horn antenna was manufactured by Millitech Inc., and its full width at half maximum (FWHM) of 8.3° is given by the antenna pattern measurement for 110 GHz (Fig. 3).

The radiation passing through the horn antenna is processed by the front end. The major purpose of the front end is to amplify the signal intensity with low noise and to convert to a lower frequency range that can be analyzed with a spectrometer. For the SORAS front end, the incident signal is amplified twice by two identical low-noise amplifiers of 18 dB. The frequency of 110.836 GHz is down-converted to the intermediate frequency (IF) of 13.750 GHz by a Gunn oscillator. The phase-locked loop (PLL) system is used to verify the 97.086 GHz frequency generated from the Gunn oscillator; the PLL uses a harmonic mixer with a 97.076 GHz signal generated from 8.0896 GHz and a 10 MHz reference signal. The IF signal is amplified, filtered, and down-converted again to 1.391 GHz. The final frequency of 0.609 GHz is established at the baseband converter in the 830 MHz bandwidth from 100 to 930 MHz.

The 0.609 GHz signal is analyzed by a digital fast-Fourier-transform (FFT) spectrometer from Acqiris AC240 (Benz et al., 2005), with a full bandwidth of 1 GHz and a frequency resolution of 61 kHz. However, the baseband converter has an asymmetrical 830 MHz bandwidth, and the actual bandwidth is determined here. As a result, considering the bandwidth of the baseband converter, the available frequency range of the received signal is limited from 110.327 to 111.157 GHz. However, random noise of unknown origin

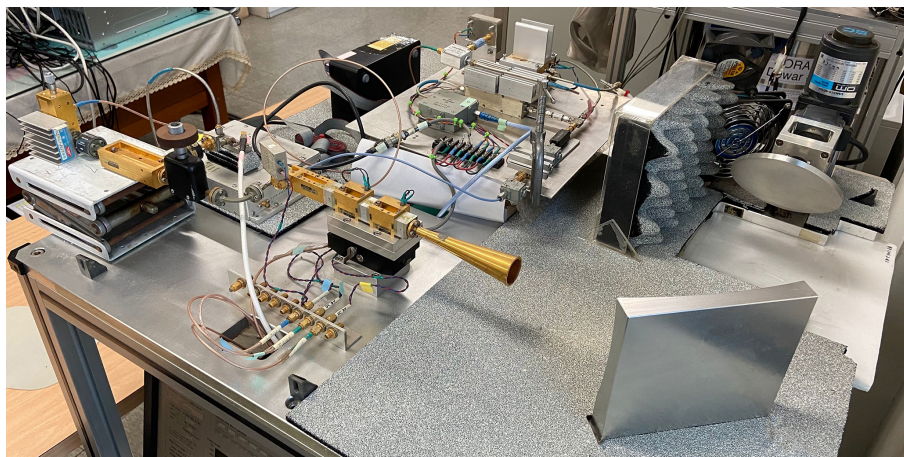


Figure 1. SORAS is in operation at the laboratory of Sookmyung Women's University, Seoul. This figure displays the quasi-optical system and the front end; the back end and the control PC are located under the front end platform.

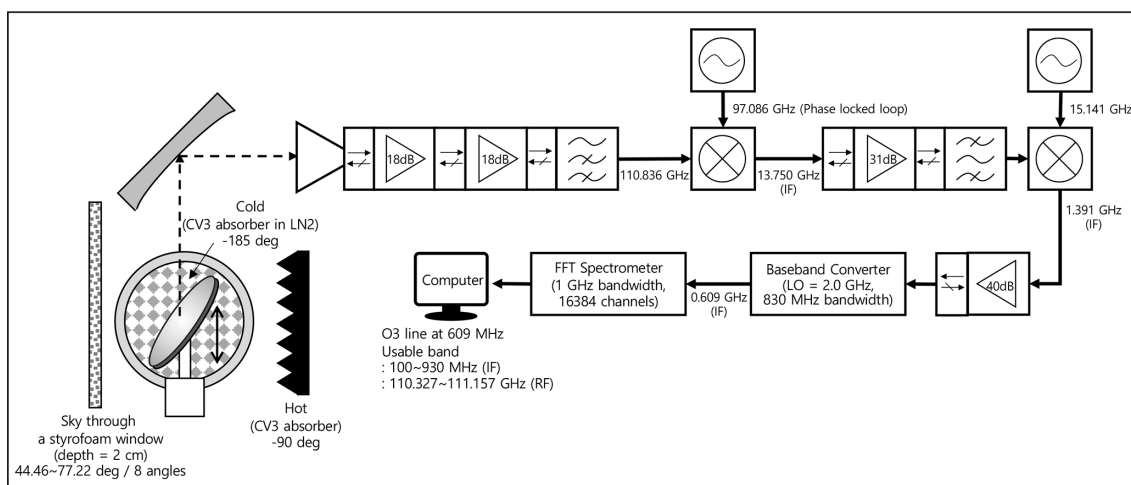


Figure 2. SORAS block diagram illustrating the quasi-optical parts with calibration targets, microwave components of the front end, and the back end with the fast-Fourier-transform (FFT) spectrometer.

was observed in the region below 110.4 GHz in the measured spectrum, and this part was excluded from the analysis in this study. Based on the observed data, the spectrum was available beyond 111.157 GHz. To ensure symmetry around 110.836 GHz, we used the spectrum ranging from 110.427 to 111.227 GHz in this study.

The additional temperature sensors connected to SORAS provide the ambient temperature and the temperature of a calibration target, which are mentioned in Sect. 3.2. The meteorological parameters such as temperature, pressure, relative humidity, precipitation, and so on are measured by the Vaisala WXT510 weather transmitter installed on the roof of the building. The system operation and data storage are controlled by LabVIEW software.

3 Measurement

3.1 Spectroscopy

The radiation frequency of atmospheric ozone is determined by the rotational transitions. However, its spectrum becomes broadened during propagation from the emitted frequency due to the collisions with other gases. The random motion of the ozone molecules also contributes to this broadening. These broadening effects are known as pressure broadening and Doppler broadening, respectively. To measure the ozone profile, we focus on the pressure broadening, which is dominant in the stratosphere and troposphere. To simulate the ozone spectrum, we must understand the absorption coeffi-

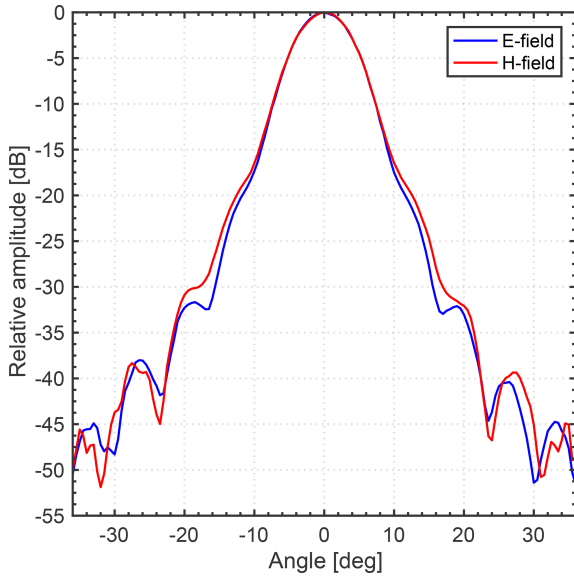


Figure 3. SORAS far-field antenna pattern at 110 GHz for the E plane and H plane.

cient α at the frequency ν :

$$\alpha_{O_3} = \sum_{i=1}^n \alpha_i(\nu), \tag{1}$$

where α_i is the absorption coefficient of i th atmospheric molecule. The α_i consists of the number density N_i , spectral intensity S_j , and line shape factor F_j at j th spectral line for the i th molecule at pressure p and temperature T .

$$\alpha_i(\nu) = N_i \sum_{j=1}^m S_j(T) F_j(\nu, p, T), \tag{2}$$

here, N_i can be calculated from the partial pressure and temperature of the gases. S_j and F_j are described well in many spectroscopic texts (Gordy and Cook, 1984; Buehler et al., 2005). Given the atmospheric profiles (pressure, temperature, and humidity) and the spectroscopic parameters from the JPL (Jet Propulsion Laboratory) or the HITRAN (high-resolution transmission molecular absorption database) catalog, we can simulate the atmospheric ozone spectrum. The ozone absorption coefficient is well-defined by spectroscopy, and we can calculate its value based on the theory. However, the rotational spectroscopy for water vapor, liquid water, and oxygen is not as well understood, spanning hundreds of gigahertz. This broad spectrum is referred to as the continuum, and the absorption coefficient has been suggested empirically by atmospheric propagation models, such as the MPM (Liebe and Layton, 1987; Liebe, 1989; Liebe et al., 1993) or Rosenkranz (Rosenkranz, 1998). As oxygen and water are concentrated in the troposphere, the continuum is often regarded as the tropospheric spectrum.

In the Rayleigh–Jeans approximation ($h\nu \ll kBT$), the atmospheric spectrum is described by the radiative transfer

equation with the absorption coefficient

$$T_b = T_{bg} \cdot e^{-\tau} + \int_0^{z_{top}} T \cdot \alpha \cdot e^{-\tau} dz, \tag{3}$$

where T_b is the brightness temperature measured at the ground, T_{bg} is the microwave cosmic background temperature of 2.7 K, and T is the temperature profile of the atmosphere. The opacity τ is the integral of absorption coefficients along the zenith path z :

$$\tau = \int_0^z \alpha(s) ds. \tag{4}$$

The atmospheric spectrum of Eq. (3) can be expressed according to the atmospheric layers by defining the weighted mean tropospheric temperature T_{trop} and the brightness temperature of the ozone T_{b,O_3} in the middle atmosphere. As the tropospheric ozone is present in very small amounts, its contribution to T_{b,O_3} can be negligible.

$$T_b = (T_{bg} + A_{mid} T_{b,O_3}) e^{-\tau_{tr} A_{tr}} + T_{trop} (1 - e^{-\tau_{tr} A_{tr}}), \tag{5}$$

where A_{tr} and A_{mid} are air masses in the troposphere and middle atmosphere, respectively, and τ_{tr} is the tropospheric zenith opacity. It should be noted that in Eq. (5), T_{b,O_3} represents the brightness temperature of ozone as observed at zenith, whereas T_b denotes the brightness temperature obtained at the measurement angle. The air mass depends on the zenith angle of the measurement, and Earth’s curvature affects the measurement, especially at high zenith angles. In this study, the air masses are calculated according to Eqs. (6) and (7), with R being the Earth’s radius (6378 km), h the tropopause height (16 km), and H the height of the middle atmosphere (84 km) (De Wachter et al., 2011).

$$A_{tr} = \frac{\sqrt{(R+h)^2 - R^2 \sin^2(\theta)} - R \cos(\theta)}{h} \tag{6}$$

$$A_{mid} = \frac{\left(\sqrt{(R+h+H)^2 - R^2 \sin^2(\theta)} - \sqrt{(R+h)^2 - R^2 \sin^2(\theta)} \right)}{H} \tag{7}$$

The T_{trop} is the weighted mean temperature of the troposphere, assumed to be a homogeneous isothermal single layer. It can be derived from the absorption coefficients by the continuum models with defined atmospheric profiles (Ingold et al., 1998).

$$T_{trop} = \frac{\int_0^h T \cdot \alpha \cdot e^{-\tau} dz}{\int_0^h \alpha \cdot e^{-\tau} dz} \tag{8}$$

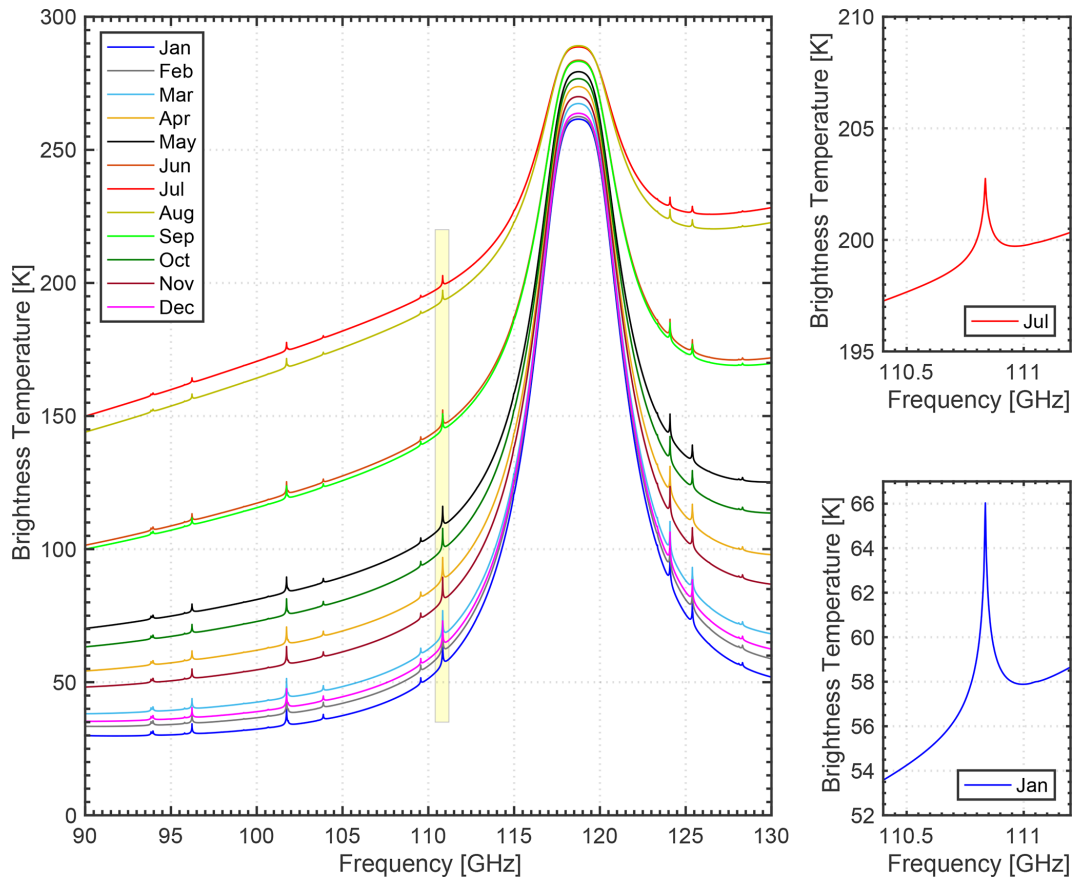


Figure 4. The atmospheric spectrum derived from monthly averaged profiles near the SORAS location, with the 110.836 GHz ozone transition line to be measured in this study highlighted.

If the frequency for the absorption coefficient is far from the ozone transition line, T_{b,O_3} in Eq. (5) can be disregarded. Consequently, T_b represents the tropospheric continuum.

The calculated atmospheric spectra in the zenith direction are shown in Fig. 4. The continuum was calculated based on the MPM93 model (Liebe et al., 1993), with the monthly averaged atmospheric profiles (pressure, temperature, and humidity) obtained from a mixture of radiosonde data at Osan, approximately 50 km away from the location of SORAS, and the AURA MLS satellite data. The ozone profiles in the middle atmosphere were taken from the MLS data. Ozone transition lines appear as spikes in the spectra, while the continuum looks like a baseline. The continuum at 110 GHz ranges from approximately 50 to 195 K due to South Korea's climate, which features hot, humid summers and cold, dry winters. The intensity of the ozone spectrum is relatively lower in July (summer) than in January (winter) owing to varying tropospheric opacity.

3.2 Calibration

In this study, the microwave radiometer is designed to measure the atmospheric spectrum at given frequencies. To con-

vert the output from the FFT spectrometer to brightness temperature, at least two reference signals emitted from loads of different temperatures, ideally blackbodies, are required. This method is known as hot–cold calibration. Using this calibration, the atmospheric brightness temperature T_b is calculated from the measurement by the following equation:

$$T_{b,\text{meas}}(\theta) = \frac{T_{\text{hot}} - T_{\text{cold}}}{V_{\text{hot}} - V_{\text{cold}}} (V_{\text{atm}}(\theta) - V_{\text{cold}}) + T_{\text{cold}}, \quad (9)$$

where T_{hot} and T_{cold} are the temperatures of calibration targets, V_{hot} and V_{cold} are the corresponding voltages from the FFT spectrometer, and V_{atm} is the voltage that measures the atmosphere at zenith angle θ . An Eccosorb[®] CV3 microwave absorber at ambient temperature is used as a hot target, and an identical absorber soaked in liquid nitrogen serves as a cold target. The receiver noise temperature has been calculated using the y -factor method (Eqs. 10, 11), and it is currently 1540 K for the SORAS system.

$$y_{\text{fac}} = \frac{V_{\text{hot}}}{V_{\text{cold}}} = \frac{T_{\text{hot}} + T_{\text{rec}}}{T_{\text{cold}} + T_{\text{rec}}} \quad (10)$$

$$T_{\text{rec}} = \frac{T_{\text{hot}} - y_{\text{fac}} T_{\text{cold}}}{y_{\text{fac}} - 1} \quad (11)$$

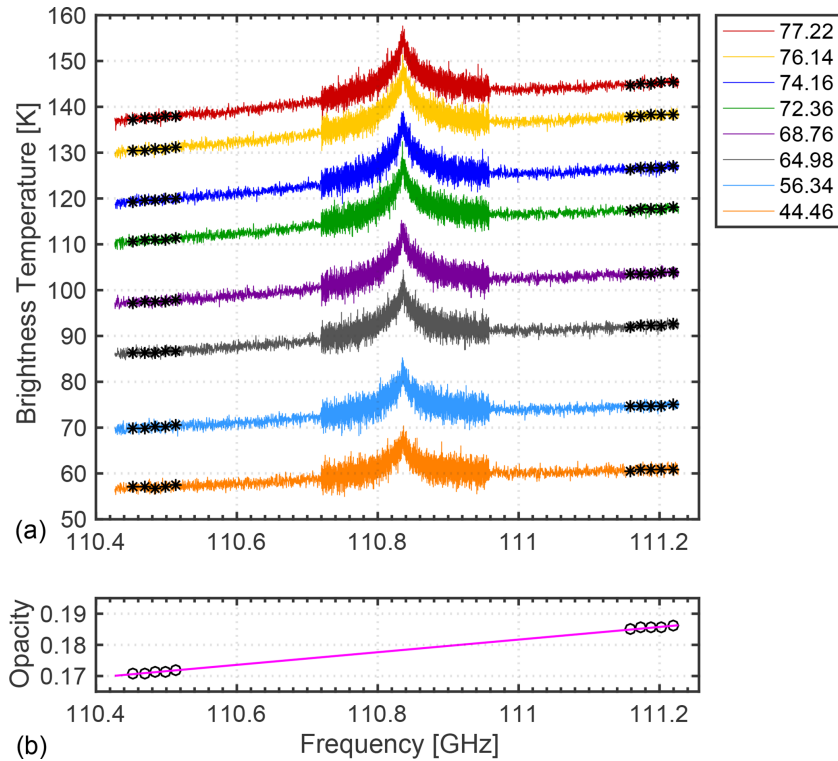


Figure 5. (a) The ozone spectrum was measured at eight different zenith angles, ranging from 44.46 to 77.22°, over a 10 min duration. The 10 black asterisks (*) on both sides of the spectrum indicate the wing regions used to calculate tropospheric opacity, as described in Sect. 3.2.4. (b) Opacity at 10 frequencies (c) was calculated from the above spectrum, along with a linear approximation of opacity over the entire frequency range (shown as a magenta line).

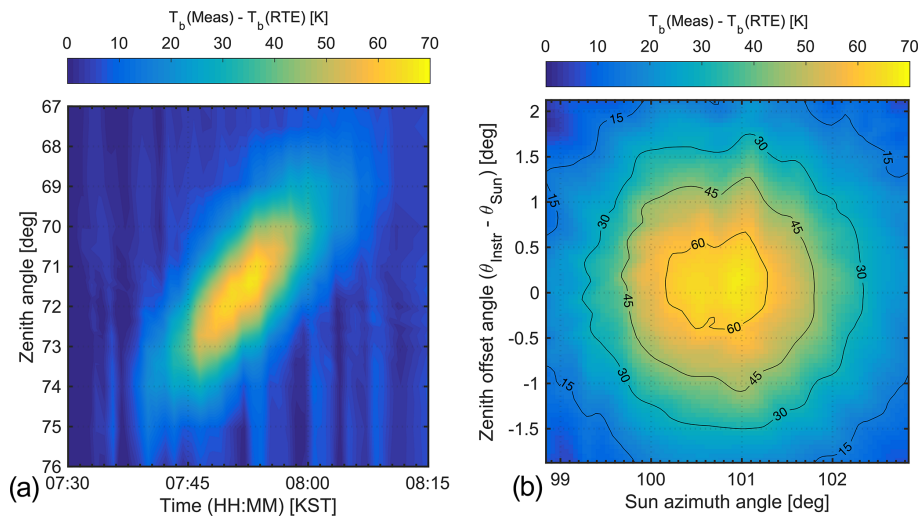


Figure 6. (a) The difference in brightness temperatures observed during the Sun scan, illustrating the Sun’s trajectory throughout the test. (b) The results presented in the left panel have been transformed relative to the Sun’s position.

3.2.1 Temperature correction

As the SORAS system is operated indoors, it observes atmospheric signals through a common styrofoam window with a thickness of 2 cm. The transmittance (t) of the styrofoam was

measured experimentally to estimate the signal loss through the window as $t = 0.997$. With the signal loss factor, the atmospheric brightness temperature is corrected from $T_{b,\text{meas}}$

by the following equation:

$$T_b = \frac{T_{b,\text{meas}} - (1-t)T_{\text{air}}}{t}, \quad (12)$$

where T_{air} is the air temperature measured by the weather transmitter installed on the roof of the building.

The temperature of the cold-calibration target is assumed to be the boiling point ($T_{\text{LN2,BP}}$) of the liquid nitrogen contained in a dewar. It is calculated using the Clausius–Clapeyron equation, considering the air pressure p (Deuber et al., 2004):

$$T_{\text{LN2,BP}} = \left[\frac{1}{T_{0,\text{LN2}}} - \left(\frac{R}{L} \right) \ln \left(\frac{p}{p_0} \right) \right]^{-1}.$$

$T_{0,\text{LN2}}$ (77.3 K) is the boiling temperature of liquid nitrogen at standard pressure p_0 (1013 hPa). R ($8.3144 \text{ Jmol}^{-1} \text{ K}^{-1}$) is the universal gas constant, and L (5660 Jmol^{-1}) is the latent heat of evaporation. The air pressure p is obtained from the weather transmitter data.

Considering the reflectivity (γ) at the surface of liquid nitrogen, the effective boiling temperature is given as

$$T_{\text{LN2}} = T_{\text{LN2,BP}}(1-\gamma) + T_{\text{amb}}\gamma, \quad (13)$$

where T_{amb} is the ambient temperature, and γ is 0.00797 (Fernandez et al., 2015a), calculated from the refractive index of $\eta = 1.196$ (Benson et al., 1983):

$$\gamma = \frac{(\eta - 1)^2}{(\eta + 1)^2}. \quad (14)$$

As the liquid nitrogen in the container is covered with a styrofoam lid, the temperature of the cold target is given by the following equation with the transmittance factor of $t = 0.997$:

$$T_{\text{cold}} = t \cdot T_{\text{LN2}} + (1-t)T_{\text{amb}}. \quad (15)$$

3.2.2 Measurement

We measured the atmospheric spectrum at eight different zenith angles ranging from 44.46 to 77.22°, with an integration time of 3.3 s for each measurement. Measurements at these angles are continuously repeated, including both hot and cold measurements. The spectra obtained from the same angle were averaged over 10 min intervals, and these averaged spectra were treated as a single measurement set (Fig. 5a). As shown in Fig. 5, the brightness temperature depends on the zenith angles because the air mass varies with the angle. The spectrometer provided spectral outputs from 16 384 channels with a resolution of 61 kHz. However, to reduce storage size, we performed binning of every five channels for the wing spectra during the data storage phase.

3.2.3 Pointing offset

The measurement of the atmospheric spectrum relies on the air mass, as indicated in Eq. (5). Since the air mass is a function of the measurement zenith angle θ , ensuring the accuracy of the zero point of the zenith angle is important. Despite the presence of a level aligner on the axis of the mirror to set this zero point, an inherent limitation exists due to the step motor's minimum step angle of 0.18°. However, we can use the Sun as a powerful point emitter for angle correction because the trajectory of the Sun is well-defined at any given geographic coordinate (Duffett-Smith and Zwart, 2011; Straub et al., 2011).

The SORAS mirror is oriented east–southeastward, so we have a chance to capture the solar emissions in the morning during certain periods. The available test period is constrained because the field of view is limited by both the physical window and the surrounding structures. Additionally, the test should be performed under a clear sky to minimize interference from water vapor and clouds. When the SORAS antenna is directed at the Sun through the opened window, there is a significant increase in measured brightness temperature. The brightness temperature, excluding solar influence, can be approximated using the radiative transfer equation with measured opacities τ_{tr} and the weighted mean tropospheric temperature T_{trop} , which will be discussed in the next section, Sect. 3.2.4.

The Sun scan measurements were conducted at 21 different angles within the zenith angle range of 65.52 to 78.48°, with an observation time of approximately 2 s per angle. Including hot and cold measurements, each set comprised 23 angles in total. Considering the mirror rotation and delay times, the observation time for one complete set was 65 s. During the 45 min observation period shown in Fig. 6, a total of 38 scans were performed. The opacity for T_b (RTE) was determined using the values observed immediately before the Sun scan.

The difference between solar brightness temperature (T_b (Meas)) and estimated non-solar brightness temperature (T_b (RTE)) gives the solar radiation pattern shown in Fig. 6. This solar radiation pattern was interpolated across zenith offset angles at a specific azimuth direction, and then it was fitted to a Gaussian curve to determine the maximum presented in Fig. 7a. To determine the pointing offset, only the data of the T_b difference larger than 25 K were considered. This analysis revealed a zenith pointing offset of 0.102° (Fig. 7b). Consequently, the zenith angle used in air mass calculations was corrected from the instrumental angle θ_{instr} to the real pointing angle θ_{SORAS} following Eq. (16):

$$\theta_{\text{SORAS}} = \theta_{\text{instr}} - 0.102. \quad (16)$$

3.2.4 Tropospheric opacity

The ozone spectrum T_{b,O_3} is reduced by the factor of $e^{-\tau_{\text{tr}}}$, as shown in Eq. (5). To restore T_{b,O_3} from the measured spec-

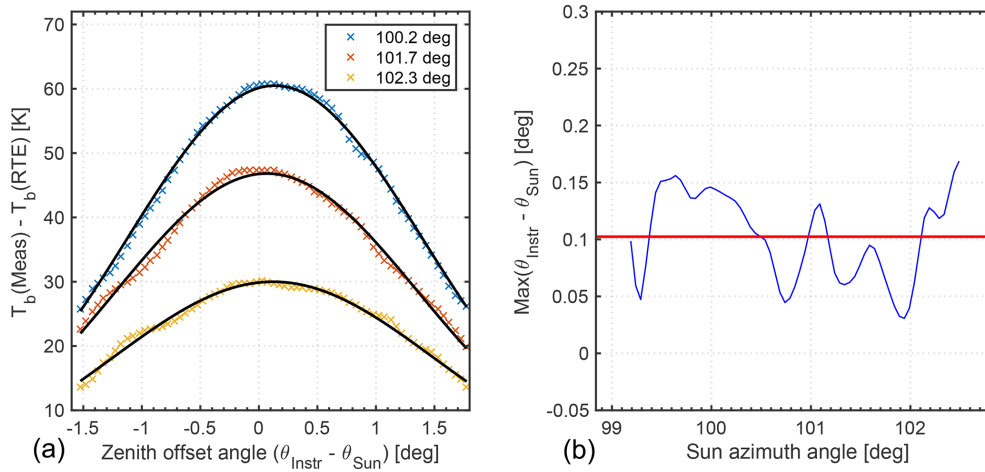


Figure 7. (a) The difference in brightness temperatures at three different azimuth angles, with the Gaussian curve fit shown. (b) The zenith offset angles from the azimuth view (in blue) alongside the averaged point offset of 0.102° (in red).

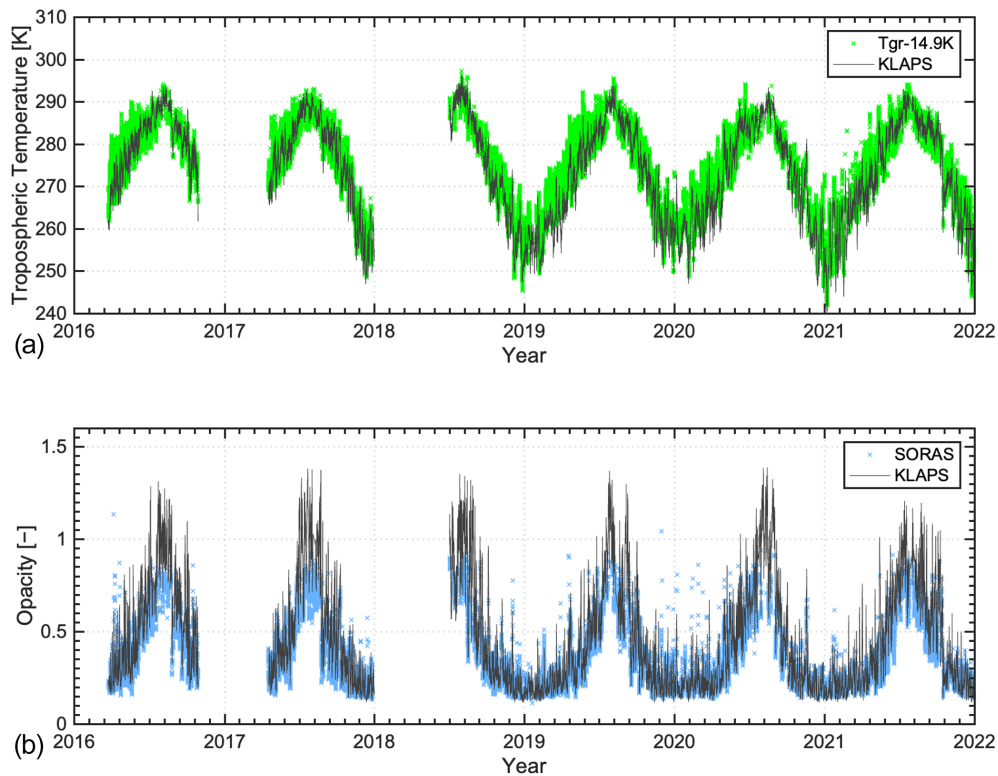


Figure 8. (a) Tropospheric temperature at 110 GHz calculated from $T_{\text{gr}} - 149$ (green circle) and derived from Eq. (8) using Korea Local Analysis and Prediction System (KLAPS) data at the SORAS location (black line). (b) Tropospheric opacities at 110 GHz, measured by the tipping curve calibration (sky blue is the 10 min interval) and calculated using KLAPS data at the SORAS location (black line is the 1 h interval). Data gaps in 2016–2017 and 2018 are attributed to hardware maintenance and sight disturbances to the measurement view, respectively.

trum T_b , we need to estimate both the tropospheric opacity τ_{tr} and the tropospheric temperature T_{trop} .

The calculation of T_{trop} from Eq. (8) is possible when the vertical profile of the pressure, temperature, and humidity is given. However, at the time of observation, sufficient infor-

mation was not available. In this study, T_{trop} was determined by adjusting the ground temperature with a factor derived from climate data. Radiosonde data from the Osan station of the Korean Air Force (37.10° N, 127.03° E, about 50 km away from the site), measured for 2 years between 2015 and

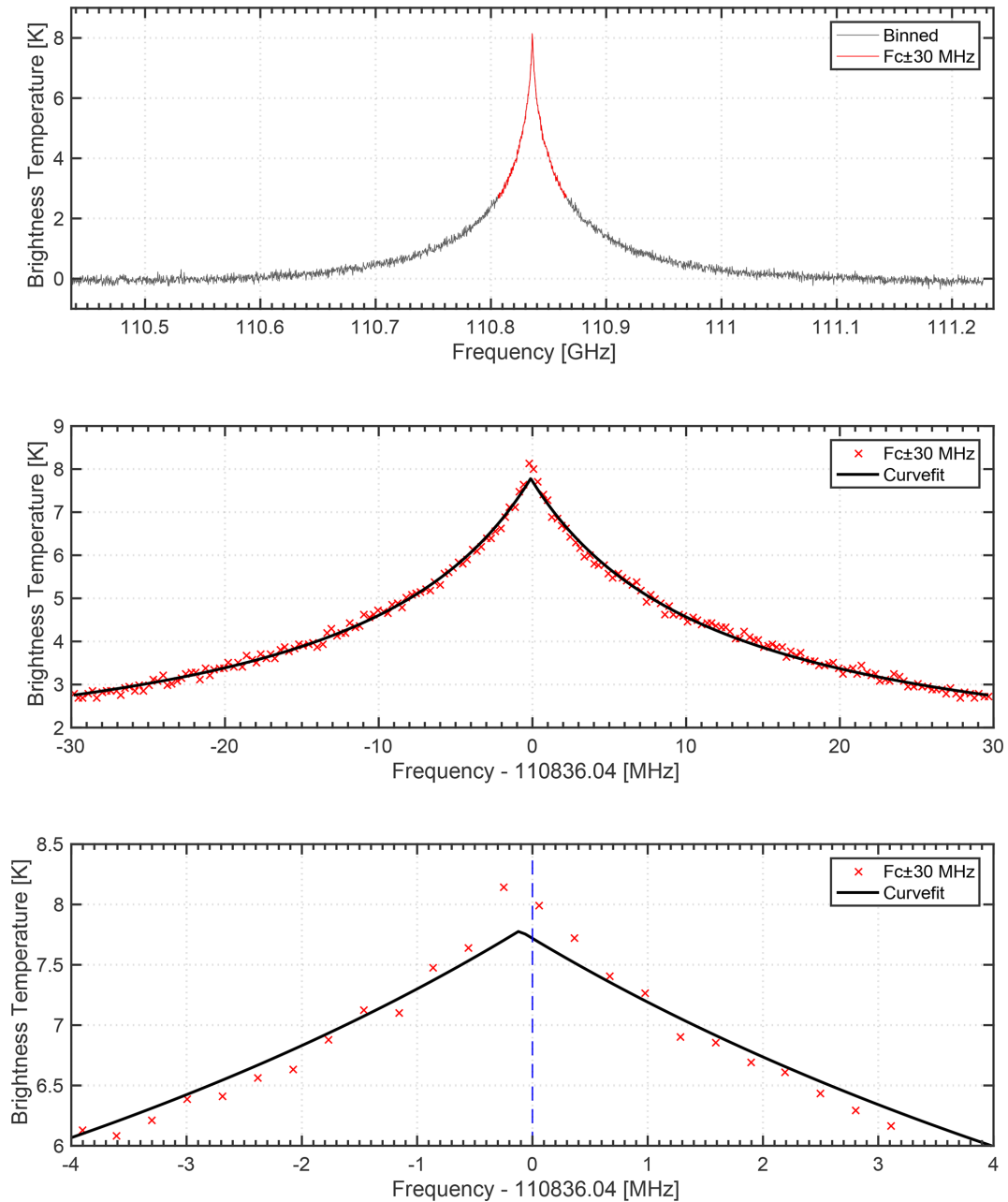


Figure 9. Procedure to determine the offset from the center frequency of the ozone spectrum. In this case, the frequency is shifted by -110.3 kHz from 110.83604 GHz.

2016, were used to calculate T_{trop} from Eq. (8). In Eq. (8), the tropopause height, h , was consistently set to 16 km throughout this period. By assuming a linear relation between T_{trop} and the ground temperature T_{gr} , we obtained the factor ΔT of -14.9 K at 110.4 GHz, which is applied to the overall frequency range of SORAS.

$$T_{\text{trop}} = T_{\text{gr}} + \Delta T \quad (17)$$

The estimated T_{trop} from Eq. (17) is compared to the T_{trop} calculated with the vertical profiles of Korea Local Anal-

ysis and Prediction System (KLAPS) data provided by the KMA (Fig. 8a). Both T_{trop} variations are comparable to each other; it turns out that the factor of -14.9 K is reasonable. It should be noted that the factor is dependent on not only the frequency but also the local climate and the altitude of the site. The value of -14.9 K is specifically applicable to 110 GHz at the SORAS location or a comparable site.

The tipping curve calibration (Han and Westwater, 2000), a general method to estimate the tropospheric opacity τ_{tr} , is performed by observing the brightness temperature T_{b} at

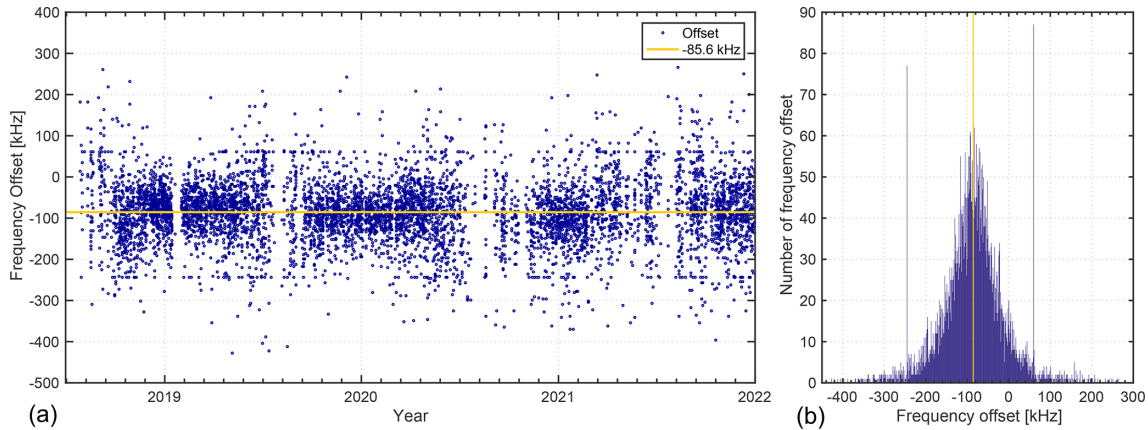


Figure 10. (a) The individual frequency offset is determined by the curve fitting method. On average, the center frequency of the measurement is shifted by -85.6 kHz from 110.836 GHz. (b) The frequency offset distribution is presented as a histogram, showing high occurrences of frequency shifts at -245 and 60 kHz.

Table 1. Parameters utilized in the SORAS retrieval.

Center frequency	110.83604 GHz
Spectroscopic catalog	JPL (for strength parameters) and HITRAN (for broadening parameters)
Atmospheric a priori	AURA MLS monthly averaged profile (2006–2015)
Frequency resolution	305 kHz (five channels binned)
Frequency bandwidth	800 MHz (110.427–111.227 GHz)
Spectrum noise level limit	≤ 0.5 K

various zenith angles θ . When T_b is measured away from the ozone transition frequency, it is reasonable to assume that T_{b,O_3} is approximately zero, allowing Eq. (5) to be rearranged as follows:

$$\tau_{tr} A_{tr}(\theta) = \ln \left(\frac{T_{trop} - T_{bg}}{T_{trop} - T_b(\theta)} \right). \quad (18)$$

Considering the nonideal homogeneity of the atmosphere, it is essential to derive a converged opacity by discarding invalid data. Equation (18) is a linear function of $A_{tr}(\theta)$ and $\ln \left(\frac{T_{trop} - T_{bg}}{T_{trop} - T_b(\theta)} \right)$ with a slope τ_{tr} intersecting at the origin. The slope τ_{tr} is recalibrated after fitting the initial dataset. Subsequently, any data deviating from the established fit line are excluded based on the presumption that such deviations are induced by atmospheric inhomogeneity. This iterative procedure ultimately yields a converged opacity value.

In this study, we measured atmospheric spectra at eight different zenith angles ranging from 44.46 to 77.22° . As shown in Fig. 5, the spectrum has a slope with respect to frequency, indicating that opacity varies with frequency within the SORAS observation range. To investigate this frequency dependence, five frequency regions on each side of the eight observed spectra were selected for opacity calculation. These frequencies were chosen from the wing regions, located 322 to 382 MHz away from the ozone frequency of 110.836 GHz. The resulting opacities at 110.46 GHz are depicted in Fig. 8b

alongside calculated opacities from KLAPS data for comparison. The opacities obtained on either side of the frequency were linearly fitted across the entire frequency range (Fig. 5b).

Now, we can deduce the ozone spectrum T_{b,O_3} from the measured brightness spectrum T_b using the tropospheric opacity τ and the tropospheric temperature T_{trop} . This results in an ozone spectrum (Eq. 19) that approximates measurements in the tropopause, even when excluding the cosmic background T_{bg} . This exclusion of T_{bg} does not significantly impact the intensity or shape of T_{b,O_3} since T_{bg} is assumed to be constant.

$$T_{b,O_3} = \frac{1}{A_{mid}} \left\{ \frac{(T_b - T_{trop}) + (T_{trop} - T_{bg}) e^{-\tau_{tr} A_{tr}}}{e^{-\tau_{tr} A_{tr}}} \right\} \quad (19)$$

4 Retrieval and validation

4.1 Spectrum setup

We acquired eight or fewer T_{b,O_3} measurements at different angles θ from a single set of observations, which are then averaged into a single spectrum for retrieval purposes. This approach aims to increase the number of measurements within a specific time frame and to minimize noise in the averaged

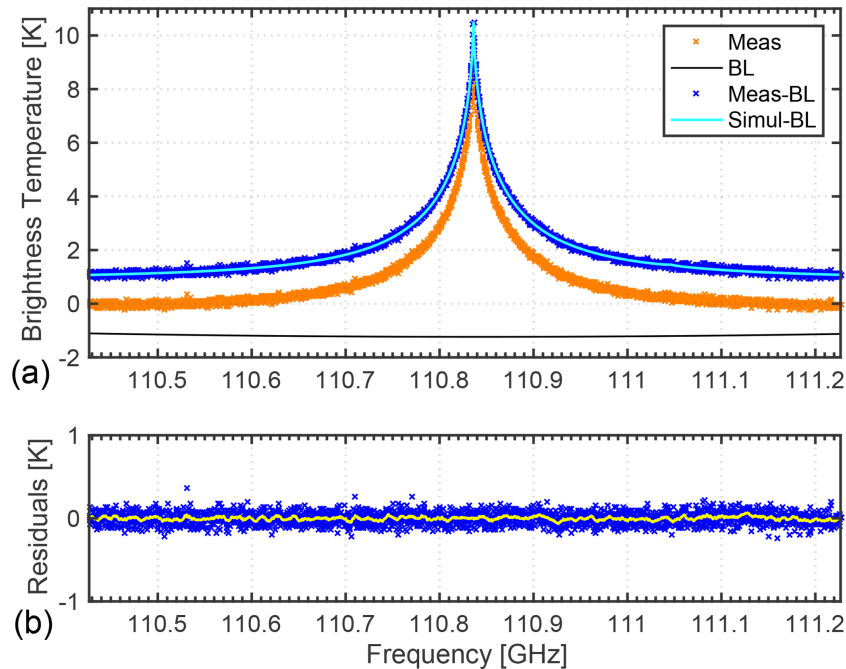


Figure 11. (a) Ozone spectrum measured over 2 h (orange and blue) alongside the simulated spectrum (cyan), with a second-order polynomial baseline (black). The measured spectrum after baseline correction is displayed in blue. (b) Residuals between measured and simulated spectra, with a smoothed line for clarity.

spectrum. The retrievals were conducted using a 2 h average of T_{b,O_3} measured from April 2016 to December 2021. Subsequently, the spectrum was binned again into five channels for the center frequency area, akin to the wings, applying a frequency resolution of 305 kHz across the entire spectrum. The retrieval spectral bandwidth is set at 800 MHz, centered around 110.836 GHz with a ± 400 MHz range. For the retrievals, only spectra with noise levels below 0.5 K are considered, which accounts for the reduced availability of profile data during summer.

The frequency (ν_{AC240}) corresponding to a channel is calculated as (Benz et al., 2005)

$$\nu_{AC240} = \frac{k}{16384} + \frac{0.5}{16384} \quad (k = 0, 1, 2, \dots, 16383), \quad (20)$$

where k represents the channels for frequencies. As $k/16384$ was defined as the lower edge of channel k , $0.5/16384$ was added to represent the center frequency of the channel. The ozone frequency of 110.836 GHz can appear to be shifted in the observed spectrum due to instabilities in the local oscillator frequency, incorrect matching between channels and frequencies, or Doppler shift. In this study, the frequency offset was determined by the curve fitting of T_{b,O_3} and corrected individually for each spectrum. Figure 9 illustrates the procedure used to identify the frequency shift for T_{b,O_3} . Following the selection of the central area around 110.836 GHz ± 30 MHz (indicated in red), curve fitting of T_{b,O_3} versus the relative frequency in MHz is performed (indicated in black), as depicted in the middle and in the bottom panels of the

figure. The offset is individually corrected prior to retrieval by adjusting the spectral frequency values. The average frequency offset observed from 2018 to 2021 was -85.6 kHz (Fig. 10). We also plotted a histogram of the offsets on the right side of Fig. 10. The histogram shows symmetry around the mean offset of -86 kHz. Upon examining the local oscillator (LO) of the baseband converter, we found that the LO frequency has a -6 kHz offset from 2 GHz, which partially contributes to a -85.6 kHz shift. However, there are significant occurrences of offsets at -245 and 60 kHz. These offsets, including the -85.6 kHz shift, appear to result from frequency shifts to specific levels caused by instability in the local oscillator at other stages of the frequency conversion, although we were unable to measure the offsets at those stages directly. Furthermore, such LO frequency shifts are likely to have a significant impact when averaging long-term observation data, which requires careful attention. The cause of the negative frequency offset could be considered a Doppler shift. However, based on previous studies (Rüfenacht et al., 2012; Hagen et al., 2018), the frequency resolution in our study is too large to measure the Doppler shift, and the lack of an opposite direction observation correction makes it insufficient to evaluate the Doppler shift. Furthermore, the spectrum used for offset analysis was a combination of spectra from eight different angles, making it unsuitable for analyzing the Doppler shift.

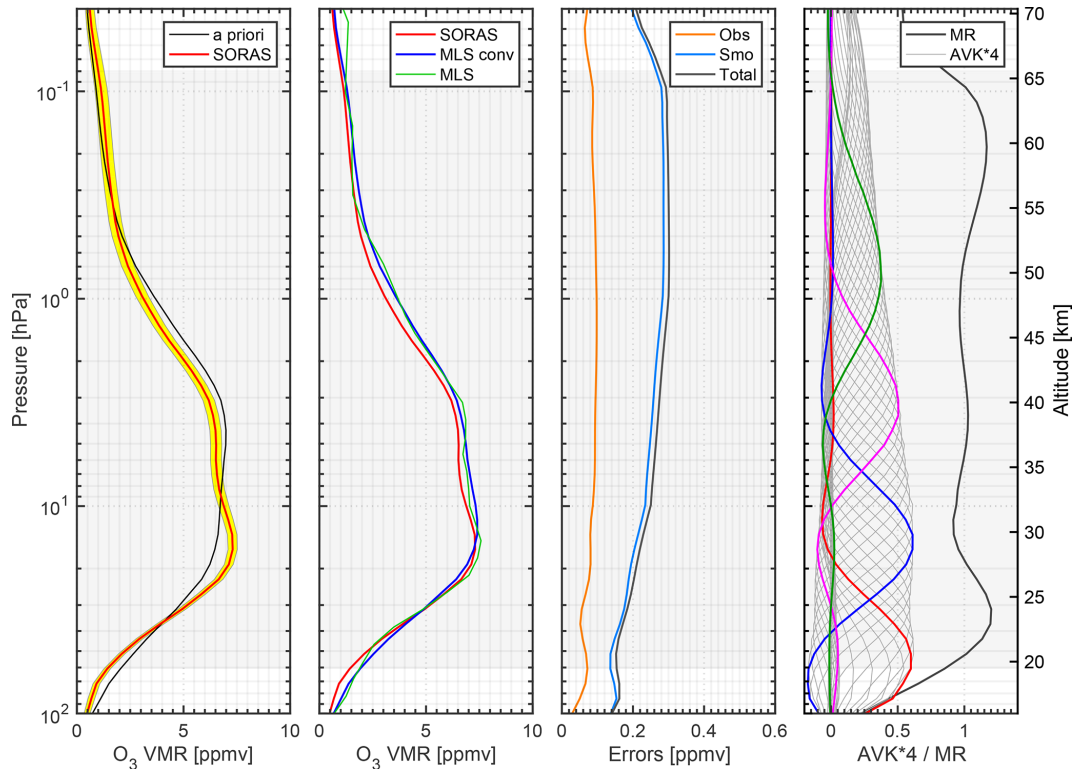


Figure 12. The ozone retrieved profile on 14 December 2019 18:00 (UTC) is presented alongside an a priori profile and total error limits. The second panel compares the MLS convolved and the original MLS profile. The third panel describes the total error, including both smoothing and observation errors. In the right panel, the averaging kernels and the measurement responses are displayed; altitudes where the measurement response exceeds 0.8 are shaded in gray. The averaging kernels at 20, 30, 40, and 50 km are presented with thick colored lines.

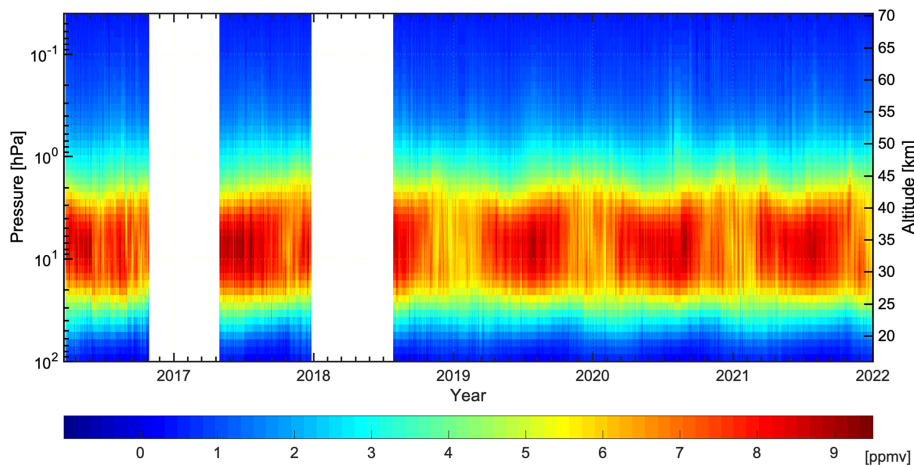


Figure 13. The SORAS microwave radiometer ozone profile measured above Seoul.

4.2 Retrieved ozone profile

The vertical profile of the stratospheric ozone is calculated through an optimal estimation method based on Bayes' theorem (Rodgers, 2000). The measured T_{b,O_3} is converted into the ozone profile for SORAS using the ARTS (v2.2) and Qpack2 software package (Eriksson et al., 2005, 2011).

ARTS simulates the spectrum by combining the continuum and molecular transitions, utilizing atmospheric radiative transfer theory (the forward model) based on the atmospheric profiles provided (also known as a priori). Qpack2 produces the optimal profile by comparing the simulated spectrum from ARTS with the measured spectrum from SO-

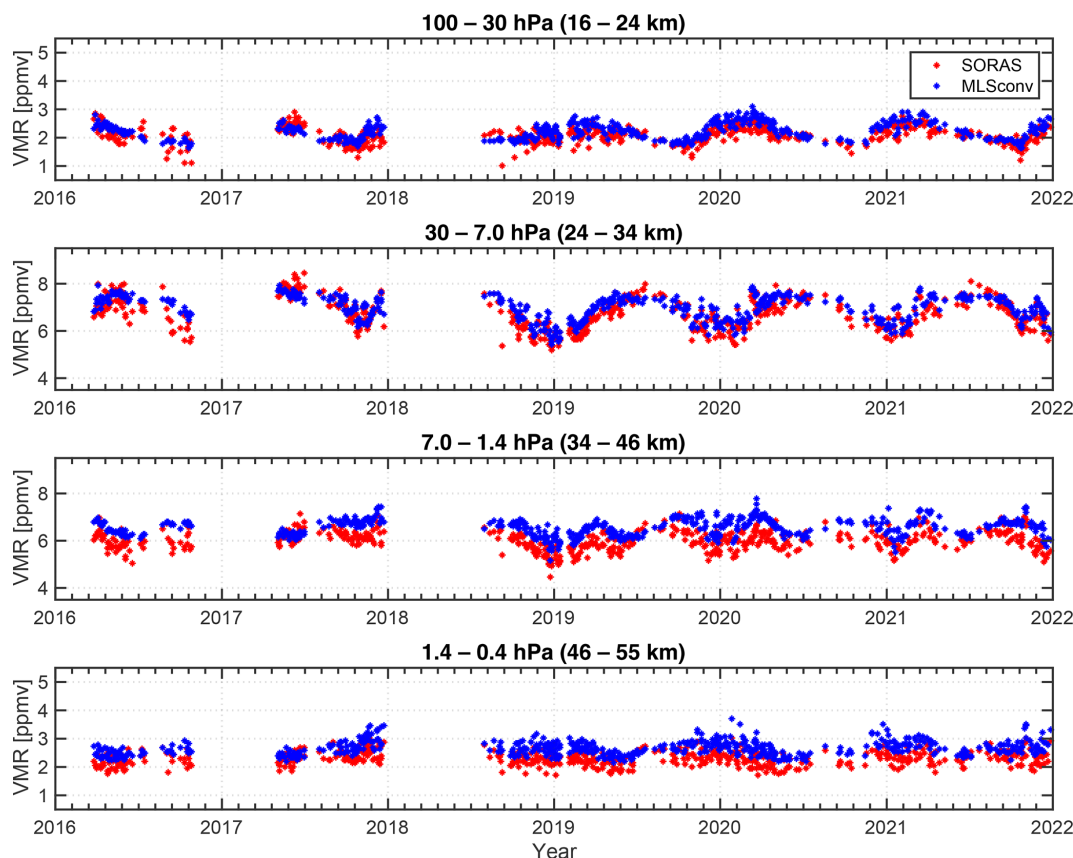


Figure 14. The ozone volume mixing ratio (VMR) above Seoul measured by SORAS (red) and MLS (blue) at four pressure levels.

RAS, considering the uncertainties in both the measurements and a priori profiles.

The main parameters for the SORAS retrieval are listed in Table 1. Spectroscopic data are compiled by combining the ozone transition information from both the HITRAN and JPL catalogs. The a priori atmospheric profiles, including stratospheric ozone, are derived from climate monthly data near Seoul, measured by the AURA MLS satellite from 2006 to 2015. Spectral noise is assumed to be constant and is determined by the standard deviation within a 9 MHz wing portion of the measured spectrum. The covariance matrix for the measurement is a diagonal matrix with elements equal to the square of the spectral noise. For the covariance matrix for the a priori profile, a Gaussian correlation function is employed between neighboring layers, setting the diagonal to a maximum value of 0.4 ppm from 10 to 1 hPa. The baseline is approximated using a second-order polynomial function.

Figure 11 shows an ozone spectrum and a simulated spectrum with its baseline. In Fig. 11a, the simulated spectrum is about 1 K higher than the measured spectrum. This difference occurs because the measured spectrum was calculated using Eq. (19), where the opacity was determined based on the wings of the measured spectrum, causing these wings to converge to zero. However, the actual spectrum observed at the

tropopause retains a certain level due to cosmic background radiation and emissions from other atmospheric molecules. This effect is corrected by applying a baseline to the spectrum. The residuals shown in panel (b) indicate no discernible pattern between the measurement and the simulation.

The retrieved ozone profile along with the a priori profile and MLS profiles is shown in the two left panels of Fig. 12. The total retrieved error is indicated by the yellow-shaded area. To account for the differing resolutions between the measurements and the MLS data, the MLS data were convolved with the averaging kernel matrix and the a priori profile of SORAS (Tsou et al., 1995).

$$x_{\text{MLSConv}} = x_a + A(x_{\text{MLS}} - x_a), \quad (21)$$

where x_{MLSConv} is the convolved profile, x_a is the a priori profile, A is the averaging kernels, and x_{MLS} is the higher-resolution MLS profile. The third panel of Fig. 12 illustrates the smoothing and measurement errors along with the total error, calculated as the square root of the sum of the squares of each individual error. In this case, the smoothing error dominates the total uncertainty across the entire altitude range.

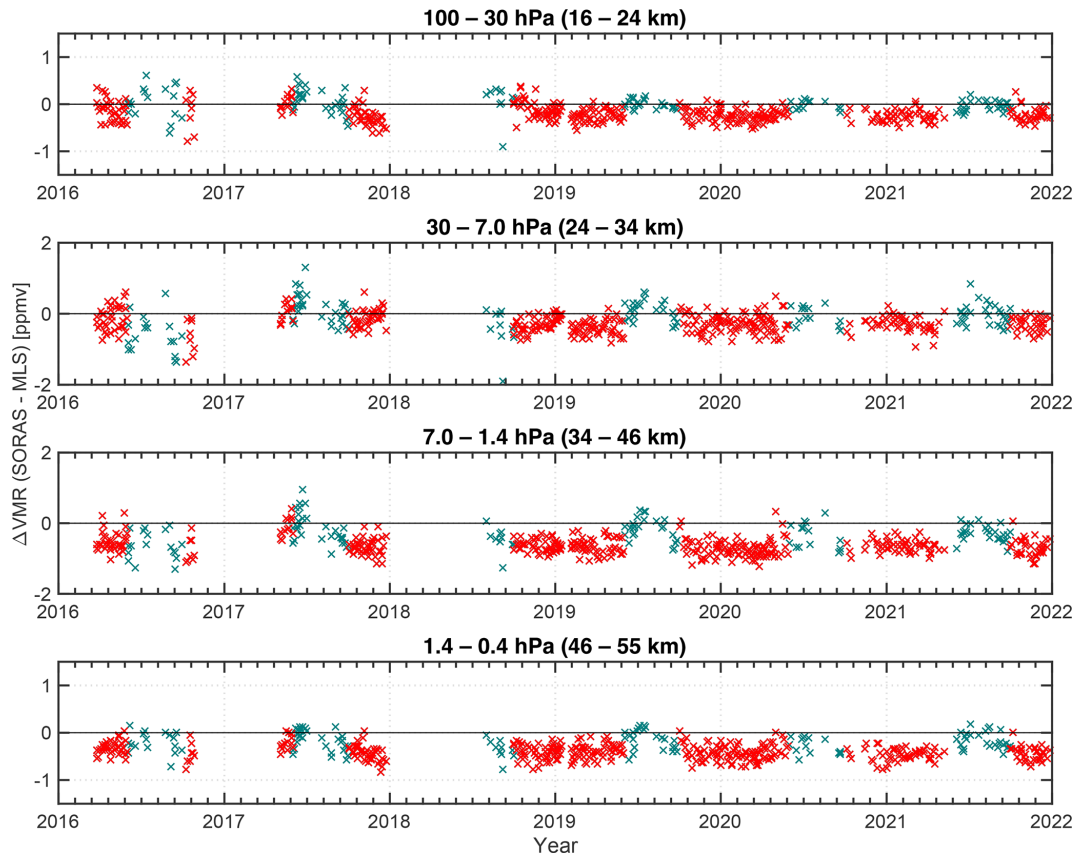


Figure 15. Difference in the ozone volume mixing ratio between SORAS and MLS convolved profiles. Red marks (×) represent data observed from January to May and October to December.

The averaging kernels and the measurement response are displayed in the right panel of Fig. 12. The altitude where the measurement response exceeds 0.8 is indicated in gray-shaded color. The measurement response quantifies the contribution of the actual measurements to the retrieved profile, as compared to the a priori profile. It is inversely proportional to the measurement noise, which is limited to a maximum of 0.5 K in our case. During the winter, when measurement noise falls below 0.1 K, the altitude range with a measurement contribution greater than 80 % extends from 60.8 to 0.08 hPa (approximately 19 to 65 km). However, in the summer season, the altitude range narrows to between 43.7 and 0.7 hPa (approximately 21 to 50 km), coinciding with noise levels exceeding 0.3 K. Figure 13 presents the ozone profiles measured by SORAS in Seoul since 2016.

Figure 14 shows the ozone volume mixing ratio measured by SORAS alongside the MLS convolved profile across four pressure intervals. The SORAS data times are confined to within ± 1 h of the MLS measurement. The difference between the two datasets is shown in Fig. 15. For most of the period, excluding summer (June to September), there is a negative bias. When comparing the opacity between SORAS and KLAPS in Fig. 8, the opacity of SORAS dur-

ing summer is lower than that of KLAPS, as shown in Fig. 16. The low calculated opacity affected the intensity by overestimating the contribution of T_{b,O_3} in the observed spectrum T_b . As a result, the comparison between SORAS and MLS led to a different bias during the summer compared to other seasons. Outside of summer, the mean biases are -0.21 ppmv (-8.8 %) at altitudes of 16–24 km, -0.27 ppmv (-4.0 %) at 24–34 km, -0.64 ppmv (-9.8 %) at 34–46 km, and -0.41 ppmv (-15.1 %) at 46–55 km. According to Sauvageat et al. (2021), these systematic biases may be attributed to unexplained spectral leakage in the AC240 spectrometer. The paper also presents ozone concentration biases at altitudes of 20–70 km, measured using the AC240 and the recent U5303 spectrometer, which range from -6 % to -11 %. These values are comparable to the biases observed in the SORAS data. However, the altitude dependence nearly disappeared when the brightness temperature with the AC240 was corrected, while the negative biases remained unchanged.

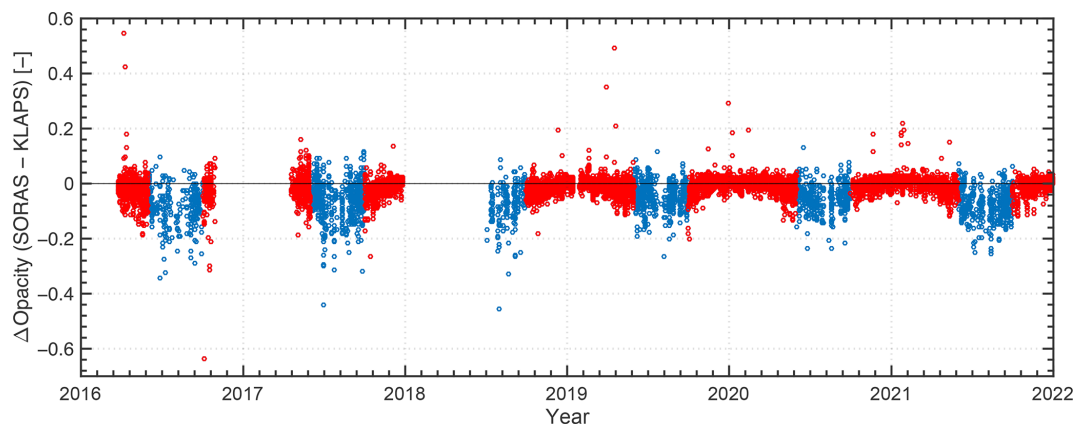


Figure 16. The difference in opacity between SORAS and KLAPS (see Fig. 8). Only SORAS data matching the time of the KLAPS data were used. The red marks are as described in Fig. 15.

5 Conclusions

SORAS is a 110.836 GHz ground-based radiometer for monitoring the vertical profiles of stratospheric ozone in Seoul. It is the first microwave radiometer developed in South Korea to measure stratospheric ozone's vertical structure. The radiometer is a heterodyne receiver, featuring a corrugated horn antenna with a full width at half maximum of 8.3° . The microwave components allow the incident radiation to be analyzed by a digital FFT spectrometer. The ozone spectrum is measured using hot–cold calibration and continuous tipping curve calibration at eight different zenith angles to estimate the tropospheric effect. The pointing offset, determined by a Sun-scanning method, is 0.102° . The weighted mean tropospheric temperature at 110 GHz is obtained by subtracting 14.9 K from the measured ground temperature.

The tropospheric contribution to the measured spectrum is eliminated prior to the retrieval. The frequency offset was corrected by fitting the curve of the spectrum and aligning the center frequency with 110.83604 GHz. The average offset is determined to be -85.6 kHz, with high occurrences of center frequency shifts observed at -245 and 60 kHz, which are presumed to result from the instability of the LO frequency. The retrieval was performed through an optimal estimation method from SORAS measurements between 2016 and 2021. The retrieved ozone profiles above Seoul are described in this paper and compared with AURA MLS convolved profiles. Excluding the summer, SORAS ozone profiles show lower values compared to MLS profiles, with differences ranging from -4% to -15% depending on the altitude. While the overall negative bias originates from the AC240 spectrometer, the altitude-dependent variation in bias is not attributed to the AC240 spectrometer.

Data availability. Data can be made available by contacting the corresponding author.

Author contributions. SK conducted the SORAS operation and data analysis and wrote the paper. JJO was responsible for the development of the SORAS and provided overall guidance and supervision for the study.

Competing interests. The contact author has declared that neither of the authors has any competing interests.

Disclaimer. Publisher's note: Copernicus Publications remains neutral with regard to jurisdictional claims made in the text, published maps, institutional affiliations, or any other geographical representation in this paper. While Copernicus Publications makes every effort to include appropriate place names, the final responsibility lies with the authors.

Acknowledgements. This study was supported by the Korea Meteorological Administration Research and Development Program under grant no. KMI2021-02510. The authors would like to acknowledge to Se-Hyung Cho from the Korea Astronomy and Space Science Institute for providing the motivation for the development of SORAS. Additionally, special thanks go to Niklaus Kämpfer and Axel Murk from the University of Bern, Switzerland, for their assistance in optimizing SORAS.

Financial support. This research has been supported by the Korea Meteorological Administration Research and Development Program under grant no. KMI2021-02510.

Review statement. This paper was edited by Dietrich G. Feist and reviewed by three anonymous referees.

References

- Ball, W. T., Alsing, J., Mortlock, D. J., Staehelin, J., Haigh, J. D., Peter, T., Tummon, F., Stübi, R., Stenke, A., Anderson, J., Bourassa, A., Davis, S. M., Degenstein, D., Frith, S., Froidevaux, L., Roth, C., Sofieva, V., Wang, R., Wild, J., Yu, P., Ziemke, J. R., and Rozanov, E. V.: Evidence for a continuous decline in lower stratospheric ozone offsetting ozone layer recovery, *Atmos. Chem. Phys.*, 18, 1379–1394, <https://doi.org/10.5194/acp-18-1379-2018>, 2018.
- Benson, J., Fischer, J., and Boyd, D. A.: Submillimeter and millimeter optical constants of liquid nitrogen, *Int. J. Infrared. Milli.*, 4, 145–152, <https://doi.org/10.1007/BF01008973>, 1983.
- Benz, A. O., Grigis, P. C., Hungerbühler, V., Meyer, H., Monstein, C., Stuber, B., and Zardet, D.: A broadband FFT spectrometer for radio and millimeter astronomy, *Astron. Astrophys.*, 442, 767–773, <https://doi.org/10.1051/0004-6361:20053568>, 2005.
- Bernet, L., von Clarmann, T., Godin-Beekmann, S., Ancellet, G., Maillard Barras, E., Stübi, R., Steinbrecht, W., Kämpfer, N., and Hocke, K.: Ground-based ozone profiles over central Europe: incorporating anomalous observations into the analysis of stratospheric ozone trends, *Atmos. Chem. Phys.*, 19, 4289–4309, <https://doi.org/10.5194/acp-19-4289-2019>, 2019.
- Buehler, S. A., Eriksson, P., Kuhn, T., von Engeln, A., and Verdes, C.: ARTS, the atmospheric radiative transfer simulator, *J. Quant. Spectrosc. Ra.*, 91, 65–93, <https://doi.org/10.1016/j.jqsrt.2004.05.051>, 2005.
- Connor, B. J., Mooney, T., Nedoluha, G. E., Barrett, J. W., Parrish, A., Koda, J., Santee, M. L., and Gomez, R. M.: Re-analysis of ground-based microwave ClO measurements from Mauna Kea, 1992 to early 2012, *Atmos. Chem. Phys.*, 13, 8643–8650, <https://doi.org/10.5194/acp-13-8643-2013>, 2013.
- De Wachter, E., Haeefe, A., Kampf, N., Ka, S., Lee, J. E., and Oh, J. J.: The Seoul Water Vapor Radiometer for the Middle Atmosphere: Calibration, Retrieval, and Validation, *IEEE T. Geosci. Remote*, 49, 1052–1062, <https://doi.org/10.1109/TGRS.2010.2072932>, 2011.
- Deuber, B., Kampf, N., and Feist, D. G.: A new 22-GHz radiometer for middle atmospheric water vapor profile measurements, *IEEE T. Geosci. Remote*, 42, 974–984, <https://doi.org/10.1109/TGRS.2004.825581>, 2004.
- Duffett-Smith, P. and Zwart, J.: Practical astronomy with your calculator or spreadsheet, 4th ed., Cambridge University Press, Cambridge, New York, <https://doi.org/10.1017/CBO9780511861161>, 2011.
- Eriksson, P., Jiménez, C., and Buehler, S. A.: Qpack, a general tool for instrument simulation and retrieval work, *J. Quant. Spectrosc. Ra.*, 91, 47–64, <https://doi.org/10.1016/j.jqsrt.2004.05.050>, 2005.
- Eriksson, P., Buehler, S. A., Davis, C. P., Emde, C., and Lemke, O.: ARTS, the atmospheric radiative transfer simulator, version 2, *J. Quant. Spectrosc. Ra.*, 112, 1551–1558, <https://doi.org/10.1016/j.jqsrt.2011.03.001>, 2011.
- Farman, J. C., Gardiner, B. G., and Shanklin, J. D.: Large losses of total ozone in Antarctica reveal seasonal ClO_x/NO_x interaction, *Nature*, 315, 207–210, <https://doi.org/10.1038/315207a0>, 1985.
- Fernandez, S., Murk, A., and Kampf, N.: Design and Characterization of a Peltier-Cold Calibration Target for a 110-GHz Radiometer, *IEEE T. Geosci. Remote*, 53, 344–351, <https://doi.org/10.1109/TGRS.2014.2322336>, 2015a.
- Fernandez, S., Murk, A., and Kämpfer, N.: GROMOS-C, a novel ground-based microwave radiometer for ozone measurement campaigns, *Atmos. Meas. Tech.*, 8, 2649–2662, <https://doi.org/10.5194/amt-8-2649-2015>, 2015b.
- Gomez, R. M., Nedoluha, G. E., Neal, H. L., and McDermid, I. S.: The fourth-generation Water Vapor Millimeter-Wave Spectrometer, *Radio Sci.*, 47, <https://doi.org/10.1029/2011RS004778>, 2012.
- Gordy, W. and Cook, R. L.: Microwave transitions-Line intensities and shapes, in: *Microwave molecular spectra*, 3rd ed., Wiley, New York, 37–70, ISBN 0471086819, 1984.
- Hagen, J., Murk, A., Rüfenacht, R., Khaykin, S., Hauchecorne, A., and Kämpfer, N.: WIRA-C: a compact 142-GHz-radiometer for continuous middle-atmospheric wind measurements, *Atmos. Meas. Tech.*, 11, 5007–5024, <https://doi.org/10.5194/amt-11-5007-2018>, 2018.
- Han, Y. and Westwater, E. R.: Analysis and improvement of tipping calibration for ground-based microwave radiometers, *IEEE T. Geosci. Remote*, 38, 1260–1276, <https://doi.org/10.1109/36.843018>, 2000.
- Hocke, K., Kämpfer, N., Ruffieux, D., Froidevaux, L., Parrish, A., Boyd, I., von Clarmann, T., Steck, T., Timofeyev, Y. M., Polyakov, A. V., and Kyrölä, E.: Comparison and synergy of stratospheric ozone measurements by satellite limb sounders and the ground-based microwave radiometer SOMORA, *Atmos. Chem. Phys.*, 7, 4117–4131, <https://doi.org/10.5194/acp-7-4117-2007>, 2007.
- Ingold, T., Peter, R., and Kämpfer, N.: Weighted mean tropospheric temperature and transmittance determination at millimeter-wave frequencies for ground-based applications, *Radio Sci.*, 33, 905–918, <https://doi.org/10.1029/98RS01000>, 1998.
- Liebe, H. J.: MPM-An atmospheric millimeter-wave propagation model, *Int. J. Infrared. Milli.*, 10, 631–650, <https://doi.org/10.1007/BF01009565>, 1989.
- Liebe, H. J. and Layton, D. H.: Millimeter-Wave Properties of the Atmosphere: Laboratory Studies and Propagation Modeling, NTIA Report 87-224, U.S. Department of Commerce, 1987.
- Liebe, H. J., Hufford, G. A., and Cotton, M. G.: Propagation modeling of moist air and suspended water/ice particles at frequencies below 1000 GHz, in: *AGARD Conference Proceedings 542: Atmospheric Propagation Effects through Natural and Man-Made Obscurants for Visible to MM-Wave Radiation*, Electromagnetic Wave Propagation Panel Symposium, Palma de Mallorca, Spain, 17–20 May 1993, 3-1–3-10, 1993.
- Maillard Barras, E., Haeefe, A., Nguyen, L., Tummon, F., Ball, W. T., Rozanov, E. V., Rüfenacht, R., Hocke, K., Bernet, L., Kämpfer, N., Nedoluha, G., and Boyd, I.: Study of the dependence of long-term stratospheric ozone trends on local solar time, *Atmos. Chem. Phys.*, 20, 8453–8471, <https://doi.org/10.5194/acp-20-8453-2020>, 2020.
- Massaro, G., Stiperski, I., Pospichal, B., and Rotach, M. W.: Accuracy of retrieving temperature and humidity profiles by ground-based microwave radiometry in truly complex terrain, *Atmos. Meas. Tech.*, 8, 3355–3367, <https://doi.org/10.5194/amt-8-3355-2015>, 2015.
- Moreira, L., Hocke, K., Navas-Guzmán, F., Eckert, E., von Clarmann, T., and Kämpfer, N.: The natural oscillations in stratospheric ozone observed by the GROMOS microwave radiometer

- at the NDACC station Bern, *Atmos. Chem. Phys.*, 16, 10455–10467, <https://doi.org/10.5194/acp-16-10455-2016>, 2016.
- Moreira, L., Hocke, K., and Kämpfer, N.: Short-term stratospheric ozone fluctuations observed by GROMOS microwave radiometer at Bern, *Earth Planets Space*, 70, 8, <https://doi.org/10.1186/s40623-017-0774-4>, 2018.
- Nedoluha, G. E., Gomez, R. M., Boyd, I., Neal, H., Parrish, A., Connor, B., Mooney, T., Siskind, D. E., Sagawa, H., and Santee, M.: Initial Results and Diurnal Variations Measured by a New Microwave Stratospheric CIO Instrument at Mauna Kea, *J. Geophys. Res.-Atmos.*, 125, e2020JD033097, <https://doi.org/10.1029/2020JD033097>, 2020.
- Newnham, D. A., Espy, P. J., Clilverd, M. A., Rodger, C. J., Seppälä, A., Maxfield, D. J., Hartogh, P., Holmén, K., and Horne, R. B.: Direct observations of nitric oxide produced by energetic electron precipitation into the Antarctic middle atmosphere, *Geophys. Res. Lett.*, 38, L20104, <https://doi.org/10.1029/2011GL048666>, 2011.
- Parrish, A., deZafra, R. L., Solomon, P. M., and Barrett, J. W.: A ground-based technique for millimeter wave spectroscopic observations of stratospheric trace constituents, *Radio Sci.*, 23, 106–118, <https://doi.org/10.1029/RS023i002p00106>, 1988.
- Parrish, A., Boyd, I. S., Nedoluha, G. E., Bhartia, P. K., Frith, S. M., Kramarova, N. A., Connor, B. J., Bodeker, G. E., Froidevaux, L., Shiotani, M., and Sakazaki, T.: Diurnal variations of stratospheric ozone measured by ground-based microwave remote sensing at the Mauna Loa NDACC site: measurement validation and GEOSCCM model comparison, *Atmos. Chem. Phys.*, 14, 7255–7272, <https://doi.org/10.5194/acp-14-7255-2014>, 2014.
- Prather, M. J.: Ozone in the upper stratosphere and mesosphere, *J. Geophys. Res.*, 86, 5325, <https://doi.org/10.1029/JC086iC06p05325>, 1981.
- Rodgers, C. D.: Inverse methods for atmospheric sounding: theory and practice, World Scientific, Singapore, <https://doi.org/10.1142/3171>, 2000.
- Rosenkranz, P. W.: Water vapor microwave continuum absorption: A comparison of measurements and models, *Radio Sci.*, 33, 919–928, <https://doi.org/10.1029/98RS01182>, 1998.
- Rüfenacht, R., Kämpfer, N., and Murk, A.: First middle-atmospheric zonal wind profile measurements with a new ground-based microwave Doppler-spectro-radiometer, *Atmos. Meas. Tech.*, 5, 2647–2659, <https://doi.org/10.5194/amt-5-2647-2012>, 2012.
- Sauvageat, E., Albers, R., Kotiranta, M., Hocke, K., Gomez, R., Nedoluha, G., and Murk, A.: Comparison of Three High Resolution Real-Time Spectrometers for Microwave Ozone Profiling Instruments, *IEEE J. Sel. Top. Appl.*, 14, 10045–10056, <https://doi.org/10.1109/JSTARS.2021.3114446>, 2021.
- Solomon, P., Barrett, J., Connor, B., Zoonematkermani, S., Parrish, A., Lee, A., Pyle, J., and Chipperfield, M.: Seasonal observations of chlorine monoxide in the stratosphere over Antarctica during the 1996–1998 ozone holes and comparison with the SLIMCAT three-dimensional model, *J. Geophys. Res.*, 105, 28979–29001, <https://doi.org/10.1029/2000JD900457>, 2000.
- Steinbrecht, W., Froidevaux, L., Fuller, R., Wang, R., Anderson, J., Roth, C., Bourassa, A., Degenstein, D., Damadeo, R., Zawodny, J., Frith, S., McPeters, R., Bhartia, P., Wild, J., Long, C., Davis, S., Rosenlof, K., Sofieva, V., Walker, K., Rahepo, N., Rozanov, A., Weber, M., Laeng, A., von Clarmann, T., Stiller, G., Kramarova, N., Godin-Beekmann, S., Leblanc, T., Querel, R., Swart, D., Boyd, I., Hocke, K., Kämpfer, N., Maillard Barras, E., Moreira, L., Nedoluha, G., Vigouroux, C., Blumenstock, T., Schneider, M., García, O., Jones, N., Mahieu, E., Smale, D., Kotkamp, M., Robinson, J., Petropavlovskikh, I., Harris, N., Hassler, B., Hubert, D., and Tummon, F.: An update on ozone profile trends for the period 2000 to 2016, *Atmos. Chem. Phys.*, 17, 10675–10690, <https://doi.org/10.5194/acp-17-10675-2017>, 2017.
- Straub, C., Murk, A., and Kämpfer, N.: MIAWARA-C, a new ground based water vapor radiometer for measurement campaigns, *Atmos. Meas. Tech.*, 3, 1271–1285, <https://doi.org/10.5194/amt-3-1271-2010>, 2010.
- Straub, C., Tschanz, B., Murk, A., and Kämpfer, N.: Scanning the Sun to determine the pointing of a 22 GHz water vapor radiometer, 2011-04-MW, Institute of Applied Physics, University of Bern, 2011.
- Straub, C., Espy, P. J., Hibbins, R. E., and Newnham, D. A.: Mesospheric CO above Troll station, Antarctica observed by a ground based microwave radiometer, *Earth Syst. Sci. Data*, 5, 199–208, <https://doi.org/10.5194/essd-5-199-2013>, 2013.
- Studer, S., Hocke, K., Schanz, A., Schmidt, H., and Kämpfer, N.: A climatology of the diurnal variations in stratospheric and mesospheric ozone over Bern, Switzerland, *Atmos. Chem. Phys.*, 14, 5905–5919, <https://doi.org/10.5194/acp-14-5905-2014>, 2014.
- Szelağ, M. E., Sofieva, V. F., Degenstein, D., Roth, C., Davis, S., and Froidevaux, L.: Seasonal stratospheric ozone trends over 2000–2018 derived from several merged data sets, *Atmos. Chem. Phys.*, 20, 7035–7047, <https://doi.org/10.5194/acp-20-7035-2020>, 2020.
- Tsou, J. J., Connor, B. J., Parrish, A., McDermaid, I. S., and Chu, W. P.: Ground-based microwave monitoring of middle atmosphere ozone: Comparison to lidar and Stratospheric and Gas Experiment II satellite observations, *J. Geophys. Res.*, 100, 3005–3016, <https://doi.org/10.1029/94JD02947>, 1995.
- World Meteorological Organization (WMO): Executive Summary. Scientific Assessment of Ozone Depletion: 2022, GAW Report No. 278, Geneva, ISBN 978-9914-733-99-0, 2022.